

Lithospheric velocity structure of the northeast margin of the Tibetan Plateau: Relevance to continental geodynamics and seismicity



Xuzhang Shen ^a, YoungHee Kim ^{b,*}, Weijun Gan ^c

^a Lanzhou Institute of Seismology, China Earthquake Administration, Lanzhou 730000, China

^b School of Earth and Environmental Sciences, Seoul National University, Seoul 08826, Republic of Korea

^c State Key Laboratory of Earthquake Dynamics, Institute of Geology, China Earthquake Administration, Beijing 100029, China

ARTICLE INFO

Article history:

Received 9 April 2017

Received in revised form 14 June 2017

Accepted 17 June 2017

Available online 19 June 2017

Keywords:

Seismic imaging

Lithospheric velocity structure

Crustal deformation

Menyuan repeating earthquakes

Northeast margin of Tibetan Plateau

Teleseismic receiver function

ABSTRACT

We provide teleseismic constraints on the continental collision zone along the SW-NE profile from the Tibetan Plateau to the Alxa block, traversing Lenglong Ling, a topographic boundary of the northeastern Tibetan Plateau. Our seismic profile crosses the Qilian Shan thrust belt, a zone of intense earthquake activity that includes a pair of M_w 5.9 earthquakes (in 1986 and 2016) with a 30-year time interval occurring at the city of Menyuan near Lenglong Ling. A high degree of similarity between the two waveforms and their similar hypocenters indicate that the two events are repeating earthquakes. Both P- and S-wave receiver functions show contrasting lithospheric structure and crustal seismic properties across the repeating earthquake region, suggesting that Lenglong Ling can be the crustal boundary between the Tibetan Plateau and the Alxa block. High-frequency P receiver functions clearly show a SW-dipping underthrust upper crust beneath the foreland of the Qilian Shan thrust belt. A strong low-velocity feature above the intracrustal underthrust beneath southwest Lenglong Ling indicates a mechanically weak zone developed coeval with the main compressional deformation during the last major tectonic event. Our observed, localized upper-crustal deformation beneath Lenglong Ling can be direct evidence of the lateral growth of the northeastern Tibetan Plateau, and can control the seismicity of the Qilian Shan thrust belt, including the Menyuan repeating earthquakes.

© 2017 Elsevier B.V. All rights reserved.

1. Introduction

The Tibetan Plateau is one of the most seismically active regions in the world, and has been actively studied to understand the relationship between the occurrence of large earthquakes and the deep crustal structures from dense array data (e.g., Nabelek et al., 2009). In the northern Tibetan Plateau, numerous large-scale faults have developed since the collision with India (Yin et al., 2008a, 2008b; Yuan et al., 2013). In particular, the Haiyuan fault is the largest strike-slip fault, which connects with the Qilian Shan thrust system and joins the Altyn Tagh strike-slip faults (Fig. 1a). These fault systems form the tectonic border of the northeastern Tibetan Plateau from the Asian blocks (e.g., Alxa and Ordos; Fig. 1a inset).

The complicated geodynamic process in the boundary region associated with the large-scale fault systems (Meyer et al., 1998; Yuan et al., 2013) has caused intense earthquake activity (Fig. 1a). Two notable large earthquakes occurred in this region, which are the M 8.3 Gulang earthquake on 23 May 1927, and the M 8.7 Haiyuan earthquake on 16 December 1920 (Gaudemer et al., 1995), the largest intraplate

earthquake ever recorded during the instrumental period. The focal mechanisms indicate that the thrust and strike-slip faulting are dominant in the Qilian Shan thrust system and the Haiyuan fault system, respectively (Fig. 1a).

On 20 January 2016, a M_w 5.9 earthquake occurred at Lenglong Ling ('Ling' means mountain ridge in Chinese) within the Qilian Shan thrust system in the northeast Tibetan Plateau (Fig. 1a). Lenglong Ling is the topographic boundary of the northeastern Tibetan Plateau. This M_w 5.9 event is only ~70 km away from the epicenter of the 1927 M 8.3 Gulang earthquake. Interestingly, its focal mechanism is identical to the one that occurred on almost the same location (~12 km west) and focal depth with the same magnitude on 26 August 1986 (Table 1; Fig. 1a). These events occurred on the fault which dips NE, based on global positioning system (GPS) measurements and focal mechanism solutions (Li et al., 2016). Also, the GPS data suggest that the epicenter region has undergone significant variation of strain (Chen et al., 2016).

The occurrence of the M_w 5.9 earthquake on 20 January 2016 raises two questions. Are these two earthquakes with a 30-year interval repeating earthquakes? If so, what are the seismic and tectonic structures that host such repeating earthquakes? If these two earthquakes ruptured the same fault segment and generate nearly identical waveforms, these earthquakes can be used to understand earthquake recurrence and fault slip rate (e.g., Stein et al., 1988), the temporal variation of

* Corresponding author.

E-mail addresses: shenxz@gsdzj.gov.cn (X. Shen), younghkim@snu.ac.kr (Y. Kim), wjgan@ies.ac.cn (W. Gan).

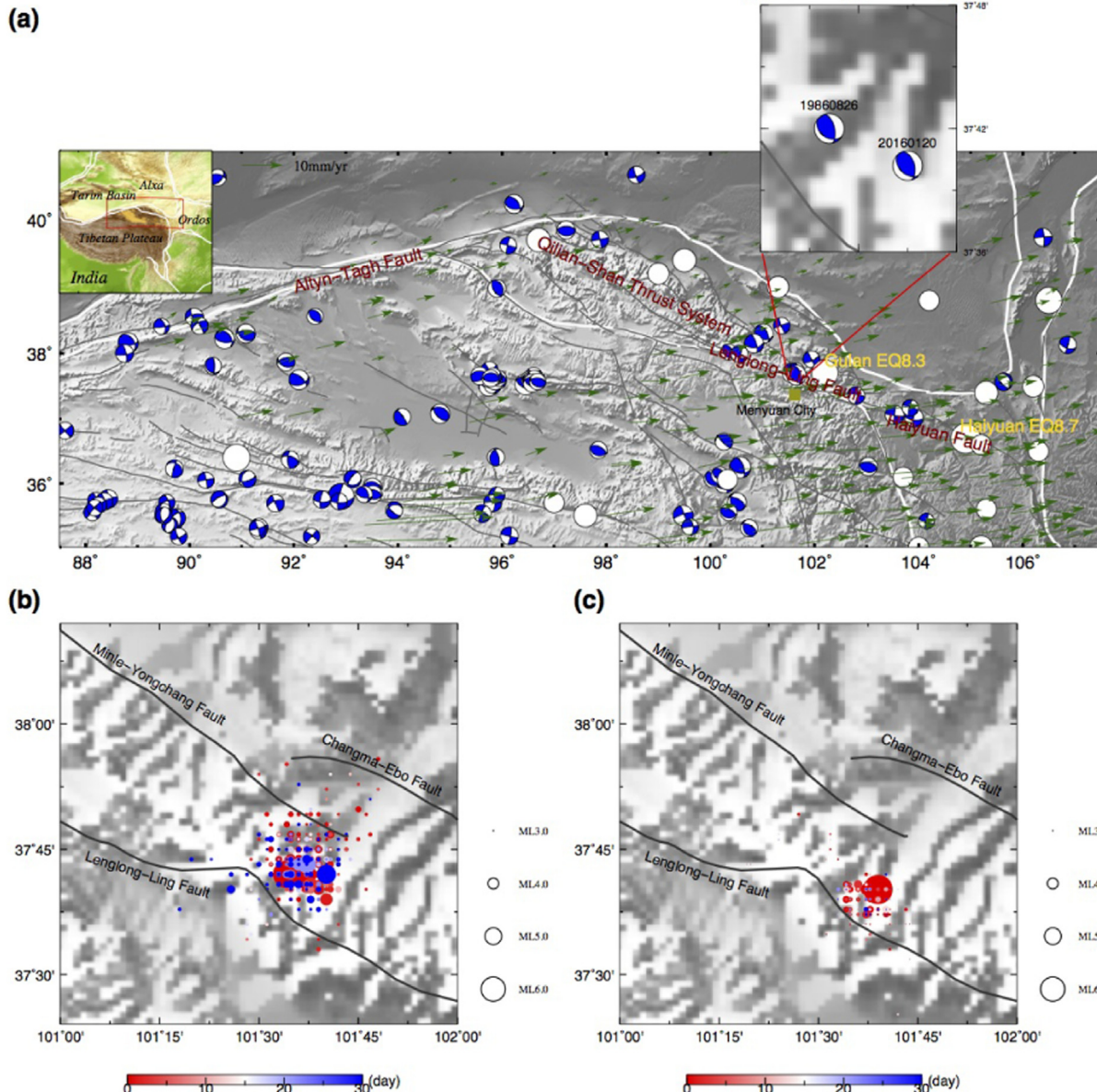


Fig. 1. Seismotectonic map showing the northeastern Tibetan Plateau. (a) Topographic and seismicity map of the study region. Thick white lines denote boundaries of major tectonic blocks (Deng et al., 2003). Gray lines show major faults in the region (Deng et al., 2003). Locations of the two M_w 5.9 earthquakes in the city of Menyuan are indicated in the top right inset. White circles denote locations of the historical earthquakes (<http://data.earthquake.cn/data/index.jsp>). Beach balls are plotted using the source parameters provided in the website of <http://www.globalcmt.org/CMTsearch.html>. Green arrows indicate the GPS vectors with a reference frame of the stable Eurasia (Gan et al., 2007; Liang et al., 2013; Chen et al., 2016). (b) Spatial and temporal distribution of aftershocks of the 1986 earthquake (<http://data.earthquake.cn/data/index.jsp>). (c) Spatial and temporal distribution of aftershocks of the 2016 earthquake (<http://data.earthquake.cn/data/index.jsp>). (For interpretation of the references to color in this figure legend, the reader is referred to the web version of this article.)

Table 1

Earthquake source parameters of 1986 and 2016 Menyuan earthquakes. The source parameters of the 1986 and 2016 earthquakes are taken from <http://www.globalcmt.org/CMTsearch.html>, and http://earthquake.usgs.gov/earthquakes/eventpage/us10004fv5#moment-tensor?source=us&code=us_10004fv5_mwc_gcmt, respectively.

EQ	Lon (°E)	Lat (°N)	Depth (km)	Mag (M_w)	NP1			NP2		
					Strike (°)	Dip (°)	Rake (°)	Strike (°)	Dip (°)	Rake (°)
1986	101.72	37.80	15	5.9	346	60	113	125	37	55
2016	101.641	37.671	13.9	5.9	343	51	109	134	43	68

Lon: Longitude; Lat: Latitude; Mag: Magnitude; NP1: Fault plane 1; NP2: Fault plane 2.

structures (e.g., Sieh, 1996; Hensch et al., 2016), and changes in fault zone properties (e.g., Vidale et al., 1994). In this study, we constrain deep seismic structure and properties beneath the source region of the two earthquakes with teleseismic receiver functions to clarify the structure and inferred relationships to seismicity, and to understand broad-scale tectonics of the plate collision zone in the northeastern Tibetan Plateau.

2. Tectonic models of the Tibetan Plateau

Various tectonic models have been put forward to explain the formation and the lateral extension of the Tibetan Plateau. In the southwestern region, the subduction of the Indian plate beneath the Tibetan

Plateau is a widely accepted viewpoint based on the results from geological investigation (Tapponnier et al., 1982, 2001; Yin and Harrison, 2000), topography (Royden et al., 1997; Clark and Royden, 2000) and seismological evidences (Kumar et al., 2006; Nabelek et al., 2009; Zhao et al., 2010). These results suggested that the eastward migration of crust and mantle material is the main reason to maintain the mass balance during the plateau uplift although their migration patterns were all different.

Based on Systeme Probatoire d'Observation dela Terre (SPOT) satellite images, Meyer et al. (1998) suggested that current crustal shortening processes in northeastern Tibetan Plateau and the growth of the plateau are controlled mainly by crustal thickening of neighboring areas. Based on GPS measurements, Royden et al. (1997) suggested that material in the lower crust flows eastwards around the Qiaodam Basin and Sichuan Basin and reaches to the eastern margin of the northeast Tibetan Plateau. Tapponnier et al. (2001) presented the lithosphere-scale deformation with several possible onsets of southward underthrusting of the Eurasia mantle lithosphere to explain observations of the sutures with different age, density and strength. Using the migration images of receiver functions from permanent seismic stations in the northeast Tibetan Plateau, Shen et al. (2015) documented that there is no significant underthrusting of the Asian lithosphere beneath

the northern Tibetan Plateau, and thus the deformation of the lithosphere can be passive and limited.

3. The 20 January 2016 M_w 5.9 earthquake at Lenglong Ling in the northeastern Tibetan Plateau

To examine if the M_w 5.9 events on 20 January 2016 and 26 August 1986 are doublet earthquakes, we compare two waveforms visually and measure their similarity (Fig. 2). The waveforms of the 1986 event are only available in analog form from ten long-period seismometers of the Incorporated Research Institutions for Seismology (IRIS) (Fig. 2c). After digitizing the analog waveforms, we apply a Butterworth filter with 0.01 to 0.05 Hz, and eliminate the influence from instrument response. Fig. 2a presents three-component waveforms of these two earthquakes recorded by the station SNZO. Arrival times of P , S and surface-wave phases for the two events are nearly identical (Fig. 2a). Fig. 2b shows vertical-component waveforms of these two earthquakes recorded by the ten stations. Values of the cross-correlation coefficients between the teleseismic waveforms exceeds 0.8, except for the station CHTO, and their average is 0.86 (Fig. 2d), suggesting high degree of similarity.

Around Lenglong Ling, there have been dozens of GPS stations measured for crustal deformation observation since 1998 (Liang et al.,

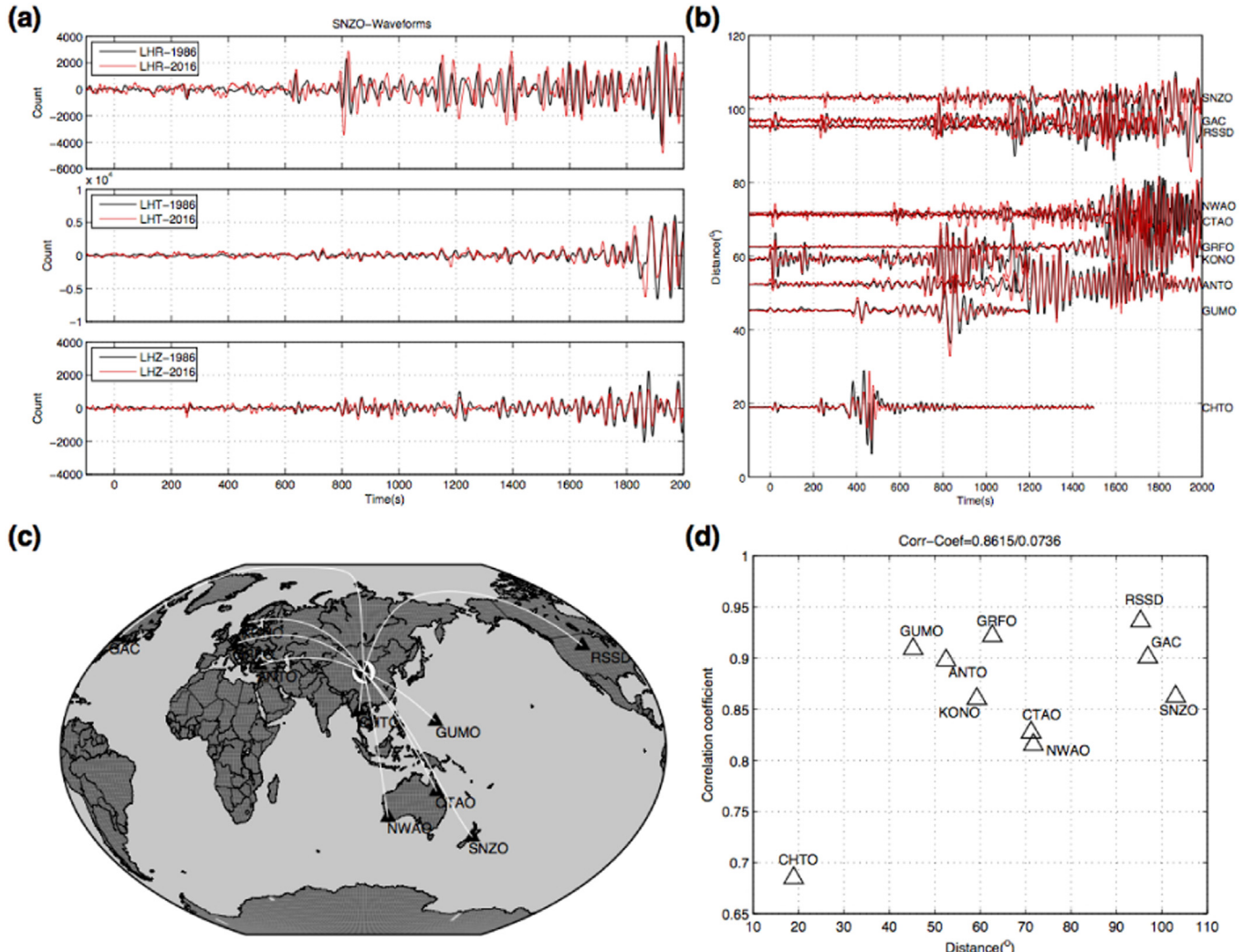


Fig. 2. Comparison of seismic waveforms of the two Menyuan earthquakes. (a) Three-component seismograms of the 1986 (black) and 2016 (red) earthquakes, recorded from a station SNZO. (b) Vertical-component seismograms of the 1986 (black) and 2016 (red) earthquakes, recorded from the stations shown in (a). (c) Map of seismic stations, which recorded the two events. (d) Cross-correlation coefficient of the vertical-component seismograms of the 1986 and 2016 earthquakes. (For interpretation of the references to color in this figure legend, the reader is referred to the web version of this article.)

2013). The GPS velocity field in the Eurasia-fixed reference frame shows that the horizontal velocities are ~6 mm/yr (NEE) and ~2 mm/yr (NNE) in the south and north of Lenglong Ling, respectively (Liang et al., 2013; Hao et al., 2014). The GPS crustal strain rate around Lenglong Ling is significantly higher than the surrounding regions, with the maximum and minimum principal strain rates of 21.5 nanostrain/yr (NW-SE extension) and –46.6 nanostrain/yr (NE-SW compression), respectively (Chen et al., 2016). Also, the direction of principal compression is consistent with the focal mechanism of the two repeating events (Chen et al., 2016).

Fig. 1b and c show spatial and temporal distribution of aftershocks of the two M_w 5.9 events. Although these events are not relocated, the aftershocks appear to be concentrated in a localized region within the Lenglong Ling fault system (Fig. 1b and c). Li et al. (2016) show relocated aftershock locations of the event on 20 January 2016, which extend down to the mid-crust (20 km depth).

4. Data and method for imaging

4.1. Data collection

A detailed investigation of structure and properties beneath the collision zone requires sufficient high-resolution geophysical data with good spatial coverage. For imaging, we collect and process teleseismic waveforms from three permanent stations and eight temporary stations, which are distributed along a SW-NE profile across the source region of the repeating earthquakes (Fig. 3a). Teleseismic event data with

magnitude exceeding 5.4 and epicentral distances of 30°–90° are collected for P -wave receiver functions, and the teleseismic events with magnitude exceeding 5.6 and epicentral distances of 60°–85° for the S -wave receiver functions (Fig. 3b).

4.2. Analysis of crustal and lithospheric velocity structure

We calculate receiver functions to examine the crust and lithosphere structures along the seismic profile. This method isolates the P -to- S or S -to- P wave conversions and reverberations generated by the discontinuities in crust and mantle by deconvolving with the incident P or S waves, respectively (Langston, 1979; Kumar et al., 2006; Yuan et al., 2006; Shen et al., 2015, 2017). Crustal thickness and average crustal P -to- S velocity ratio (V_p/V_s) beneath each station are obtained by stacking Ps , $PpPs$, and $PpSs + PsPs$ phases on the radial-component P receiver functions. The P receiver function may not be ideal for investigating lithospheric discontinuities such as the lithosphere-asthenosphere boundary (LAB) because of the interference with seismic multiples from the Moho and/or shallower structures (Yuan et al., 2006). On the other hand, the S receiver function has some advantages detecting the lithospheric discontinuities including LAB because the S -to- P phases from such deep discontinuities arrive much earlier than the multiples from the shallow discontinuities. A detailed calculation of the receiver functions can be found in our previous work (Shen et al., 2017).

We obtain 1530 P receiver functions and 1023 S receiver functions. The pierce points of both P and S receiver functions at the Moho depth are plotted in Fig. 3a. Raw receiver functions are filtered by a

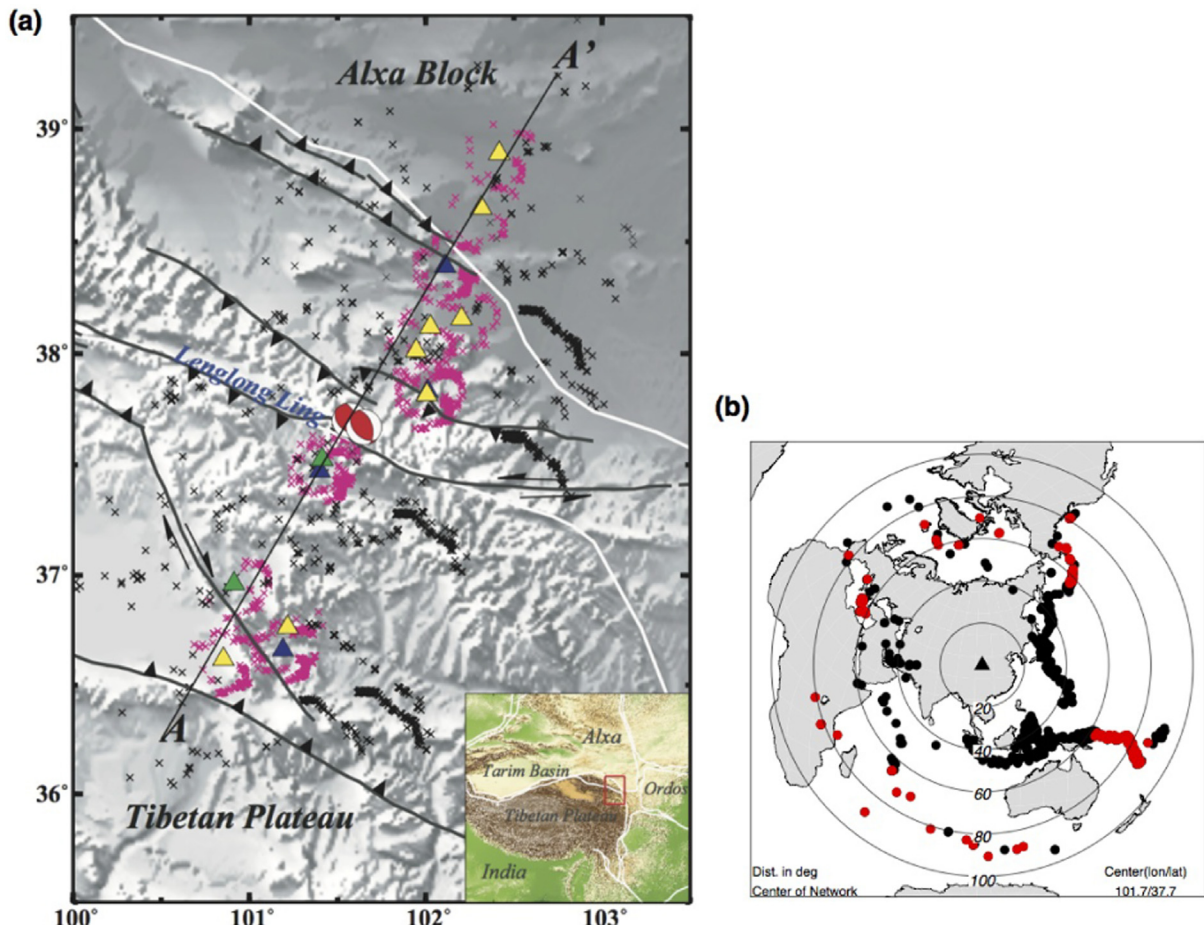


Fig. 3. Map showing seismic stations and teleseismic earthquakes for receiver functions. (a) Locations of temporary stations (yellow-ZV; green-XD) and permanent stations (blue), shown on the topographic map. The fault locations are taken from Yuan et al. (2013). Pierce points for P -to- S and S -to- P conversions from the Moho are shown as pink and black crosses, respectively. (b) Map of teleseismic events used in this study. The triangle indicates the centroid location of the seismic network. Black and red dots are the events used for P and S receiver functions, respectively. (For interpretation of the references to color in this figure legend, the reader is referred to the web version of this article.)

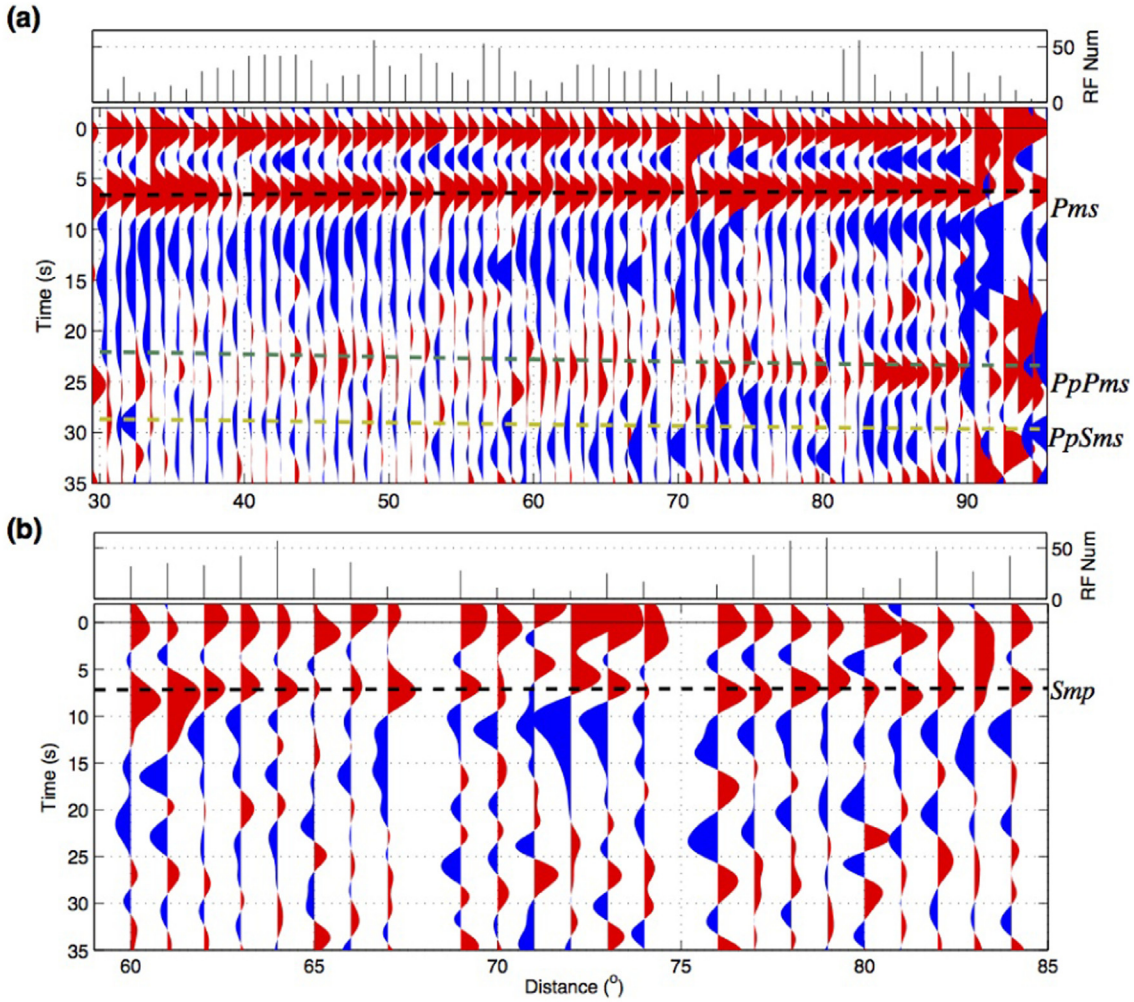


Fig. 4. Stacks of P receiver functions (a) and S receiver functions (b) aligned by the epicentral distance. The receiver functions are binned within 1° distance, and the number of the receiver functions to make a single trace is shown on the top. The dashed black lines indicate converted phases from the Moho ($P_{m\text{s}}$ on P receiver functions in (a), and $S_{m\text{p}}$ on S receiver functions in (b), where ‘ m ’ denotes the Moho). Clear seismic multiples ($PpP_{m\text{s}}$ and $PpS_{m\text{s}}$) are shown in the P receiver function stacks, and their arrivals are indicated as colored dashed lines. (For interpretation of the references to color in this figure legend, the reader is referred to the web version of this article.)

Butterworth band filter with 5–50 s, and then are aligned by an epicentral distance (Fig. 4). Consistent positive-amplitude arrivals of $P_{m\text{s}}$ and $S_{m\text{p}}$ (where ‘ m ’ denotes Moho) at about 7 s demonstrate the reliability and stability of both P and S receiver functions.

The resulting individual receiver functions are migrated to a depth along the profile using common conversion point (CCP) stacking. This method retraces the receiver functions to the ray path, and converts the time series of the receiver functions into the spatial domain. For a given profile, horizontal and vertical windows are moved with 1 km step, and the receiver functions with the pierce points within one-half Fresnel’s zone are selected to stack (Shen and Zhou, 2009). Fig. 5a and b show the migration images of the P and S receiver functions, respectively. Along the profile, the limited coverage of the ray path and station distribution cannot well resolve detailed features of the uppermost crust within ~ 10 km (Fig. 5a).

In order to investigate detailed structures within the crust, we apply a high-frequency band-pass filter with 1–50 s to the raw P receiver functions, and align stacked receiver functions after applying Ps moveout correction with 0.025° step along the A-A' profile (Fig. 3a). The receiver functions within the neighboring 4 bins, weighted by the inverse square of the distance, are used to smooth the stacking results (Fig. 6a).

The arrivals of $P_{m\text{s}}$ and $PpP_{m\text{s}}$ phases can be used to constrain an average value of crustal thickness (H) and V_p/V_s (κ). To measure their arrival times precisely, we correct the P receiver functions for distance moveout according to $P_{m\text{s}}$ and $PpP_{m\text{s}}$ phases using a reference slowness

of $6.4 \text{ s}/^\circ$ based on the IASP91 model (Kennett and Engdahl, 1991). The moveout-corrected receiver functions are stacked in 0.1° latitude bins of pierce points, which can ensure the stability of stacking results. We then select the maximum around visibly clear $P_{m\text{s}}$ and $PpP_{m\text{s}}$ phases (circles shown in Fig. 7a and b, respectively) to measure their arrival times, and these data are used to compute H and κ with an average V_p of 6.2 km/s (Shen et al., 2011) along the profile. The bootstrap resampling method (Efron and Tibshirani, 1998) is used to estimate errors of the arrivals of $P_{m\text{s}}$ and $PpP_{m\text{s}}$ phases (Fig. 7), and then these errors are mapped onto uncertainty estimates of H and κ (Fig. 8).

5. Results

Migration images down to 200 km depth (Fig. 5a and b) along the A-A' profile (Fig. 3a) show topographic and seismic velocity variations of crustal and lithospheric discontinuities across the repeating earthquake region. In particular, positive-amplitude Ps signals (at 6–7 s, shown in Fig. 4) for Moho are clear in the migration image of both P and S receiver functions around 50 km depth. We extract the Moho depth as a black dashed line from the P receiver-function image (Fig. 5a), and copy it to the migration image of the S receiver functions (Fig. 5b). The consistency of the Moho depth estimates from the different teleseismic phases indicates the stability and reliability of our results.

The Moho sits deeper at ~ 60 km in the SW of Lenglong Ling, and shallower at ~ 50 km in the NE of Lenglong Ling (Fig. 5a and b). To the

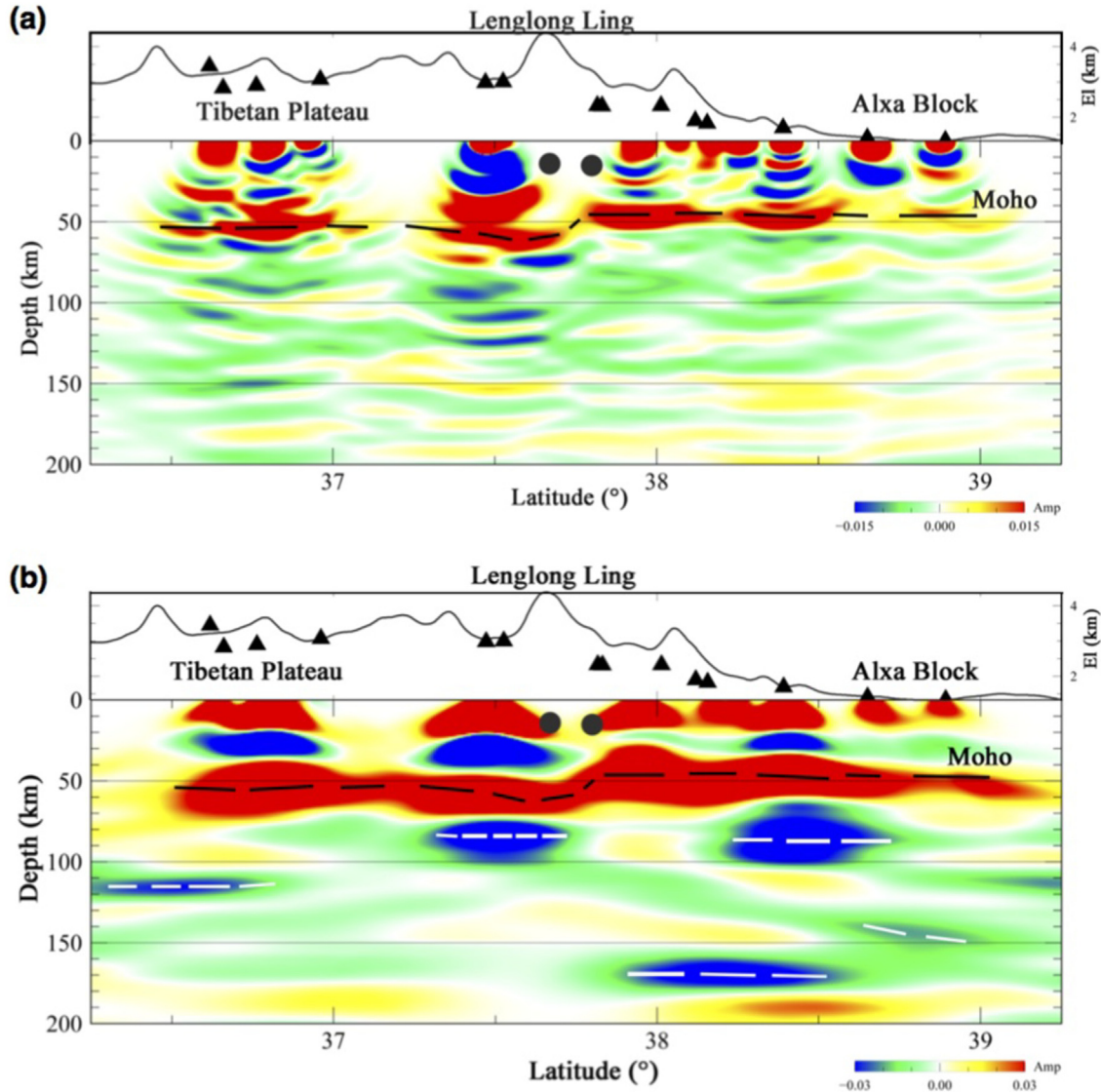


Fig. 5. Common conversion point (CCP) images along the seismic profile. (a) Migration image from P receiver functions. (b) Migration image from S receiver functions. Topography along the profile is indicated in the top panel. The black dashed line for the Moho is extracted from the P receiver-function image, and copied to the S receiver-function image. Strong S-to- P amplitudes are marked with the white dashed line in the S receiver-function image. The repeating earthquakes are marked with dark gray circles beneath Lenglong Ling.

west of our profile, ~10–20 km thickness change in crustal thickness is observed along a SW-NE direction (Zheng et al., 2016). Along the A-A' profile (Fig. 3a), the sharp transition in the crustal thickness occurs at Lenglong Ling (Fig. 5).

From the NE to SW of Lenglong Ling, ~100 km laterally (Fig. 6a, black dashed line), we recognize SW-dipping, positive-amplitude signals around 20–30 km depth within the crust, which might represent a mid-crustal layer (underthrust interface) between the upper and mid-lower crust. The first-arriving multiple from this SW-dipping interface ($PpPds$, where 'd' denotes a discontinuity) is somewhat visible (Fig. 6a, green dashed line), although its later multiple ($PpSds$) is weak. Also, a termination of this interface in the region SW of Lenglong Ling is not clear in the image (Fig. 6a). The similar interface has been reported in the northern front of the Qilian Shan thrust belt, which sits in the west of our study region, from wide-angle reflection and refraction studies (Zeng et al., 1998; Gao et al., 1999).

In addition to the imaged sharp transition in the crustal thickness across Lenglong Ling, we observe strong and more complex signals close to the SW of Lenglong Ling, which are observed before the coherent signals from Moho (Figs. 5a and 6a). The clearest signals are consistent negative amplitudes (at 2–3 s) that arrive after the P phase near 0 s

(Fig. 6a). These signals dip towards the NE, and their amplitude strength decreases towards the NE. The strongest negative-amplitude signals are observed SW of Lenglong Ling for the region around 37.5° latitude (Fig. 6a, gray bar) with their amplitudes larger than half of Pms amplitudes at 6 s. We note that the repeating earthquake locations are closely associated to the region with negative-amplitude signals (Fig. 6a).

We modeled selected 14 P receiver functions with such strong negative amplitudes at 2–3 s (Fig. 6a, gray bar) for filter ranges of 1–50 s and 3–50 s as shown in Fig. 6b and c, respectively, to constrain the optimal shear wave velocity profile and layer thicknesses within the crust SW of Lenglong Ling. Both receiver-function sets have P -to- S piercing points at 60 km-depth discontinuity at the latitude range of 37.45° – 37.55° . The best fitting velocity model is shown in Fig. 6d and e. This model includes a relatively thin (3 km) low-velocity layer at ~17–20 km in the upper crust (Fig. 6d), which constrains the observed large negative-amplitude signals at 2–3 s (Fig. 6a). The thin low-velocity layer has V_s of 2.5 km/s and V_p/V_s of 2.0 (Fig. 6d and e). The V_p and V_s of the layer are lowered by 2.4% and 21.9% with respect to V_p and V_s of the layer above, respectively. In addition, we find other negative-amplitude signals (at 3–4 s) that immediately follow the strong negative-amplitude signals SW of Lenglong Ling, which are enclosed in a dashed box in Fig. 6a. These

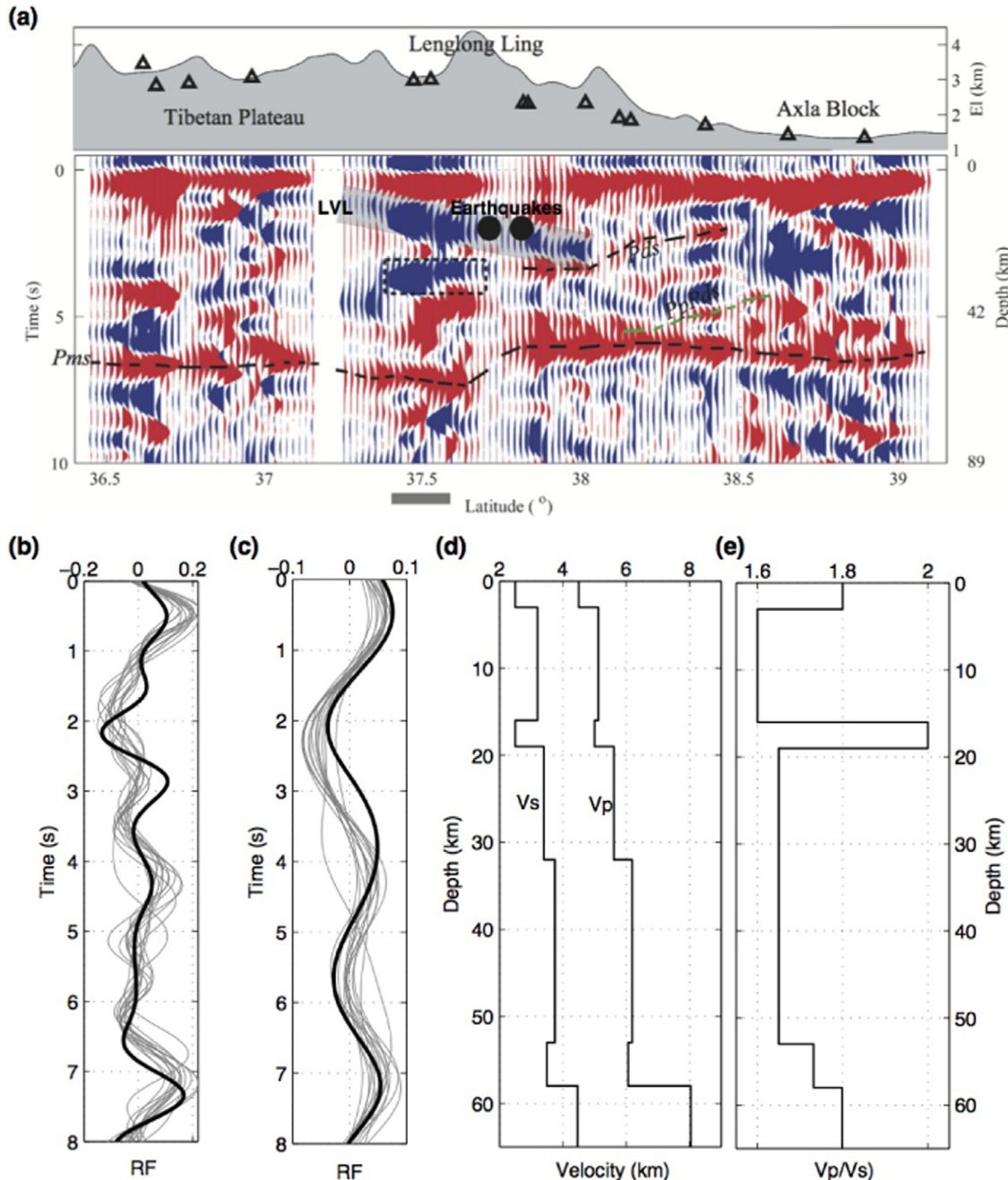


Fig. 6. Stacked high-frequency P receiver functions and receiver-function waveform modeling results. (a) Stacks of high-frequency (1 s) P receiver functions after applying the moveout correction for Ps . The triangles on the topography represent seismic stations used. The numbers on the right correspond to depths estimated from Ps arrival time. The black dashed line along the whole profile marks Pms phase for Moho, and the dashed line beneath the NW region of Lenglong Ling marks a SW-dipping interface (Pds) within the crust. The first multiple ($PpPds$) of this SW-dipping interface is marked with a green dashed line. The low-velocity zone beneath Lenglong Ling is highlighted as a gray shaded zone. The negative signals (black dotted box) present below the low-velocity zone may represent possible multiples from shallow structures. (b) Observed (thin gray lines) and synthetic (a thick black line) receiver functions at 1–50 s. (c) Observed (thin gray lines) and synthetic (a thick black line) receiver functions at 3–50 s. (d) V_p and V_s profiles of the model. (e) V_p/V_s profile of the model. (For interpretation of the references to color in this figure legend, the reader is referred to the web version of this article.)

signals can be explained by the reverberated phases originating from near-surface structures under the region.

Our analysis results show the contrasting crustal thickness and V_p/V_s along the seismic profile across Lenglong Ling. The crust is relatively thicker (~57–64 km) with lower velocity ratios (range 1.587–1.710 with an average and standard deviation of 1.655 ± 0.040 ; Poisson's ratio of 0.171–0.240) beneath the Tibetan Plateau, while thinner (~44–52 km) with higher velocity ratios (range 1.684–1.811 with an average and standard deviation of 1.744 ± 0.038 ; Poisson's ratio of 0.228–0.281) beneath the Axla block (Fig. 8a). This observation is consistent

with previous results based on the data from permanent seismic stations in other regions in and near the northeastern Tibetan Plateau (Wang et al., 2010; Pan and Niu, 2011; Shen et al., 2011; Tian and Zhang, 2013; Tian et al., 2014). Our data can be fitted by a linear line, $\kappa (V_p / V_s) = 2.1721 - 0.0088H$ (Fig. 8b).

In addition, the negative-amplitude signals are observed between depths of 70–170 km in the migration image of the S receiver functions (Fig. 5b), and the clearest signals are marked with white dashed lines. These represent the S -to- P conversions from the lithospheric discontinuities. The S -to- P conversion is observed particularly strong with

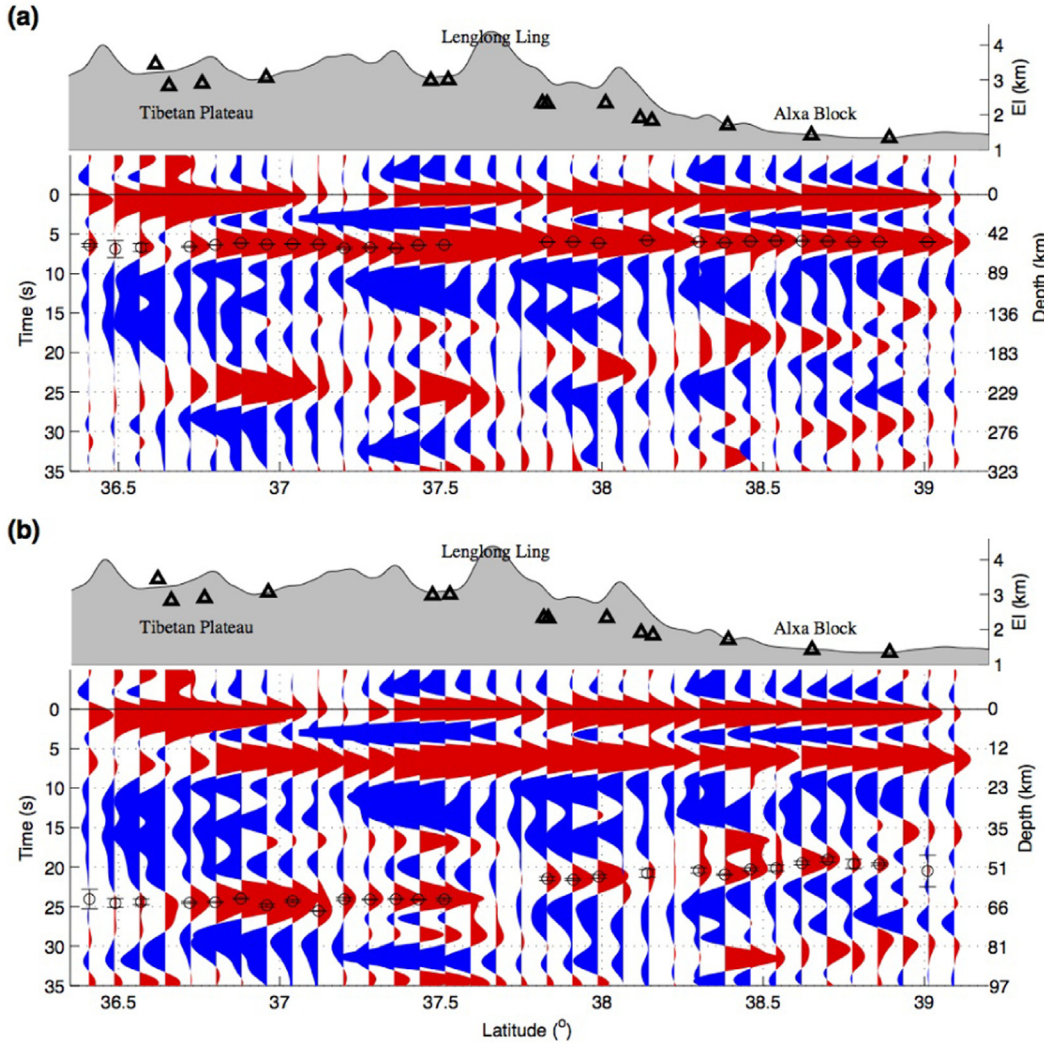


Fig. 7. Profiles of moveout corrected, stacked P receiver functions along the seismic profile. (a) Ps moveout corrected receiver functions. The arrivals of Pms are marked with circles. (b) $PpPs$ moveout corrected receiver functions. The arrivals of $PpPms$ are marked with circles. Note that only the arrivals with clear Pms and $PpPms$ phases are marked in the images. The numbers on the right side of each image indicate to the depth estimated by P -to- S arrival time.

large depth variation beneath Lenglong Ling and the region NE of Lenglong Ling, but somewhat weaker beneath the Tibetan Plateau (Fig. 5b). This observation is in line with previously reported results, which suggest that the lithospheric discontinuities beneath the Tibetan Plateau are less clear, whereas they are shown sharp beneath the Asian blocks (Shen et al., 2015, 2017). The observed contrast in terms of both depth and receiver-function amplitudes of the lithospheric discontinuities roughly coincide the region under the topographic boundary of the northeastern Tibetan Plateau and also the repeating earthquake region (Fig. 5b).

6. Discussion

6.1. Crustal and lithospheric velocity structure

Along the A-A' profile (Fig. 3a), the sharp transition in the crustal thickness occurs beneath Lenglong Ling (Fig. 5a). This observation suggests that Lenglong Ling can be the crustal boundary between the Tibetan Plateau and the Alxa block in our study region. In addition to the imaged sharp transition in the crustal thickness across Lenglong Ling, we observe strong and more complex signals near the SW of Lenglong Ling (Figs. 5a and 6a). The strong negative-amplitude signals indicate a presence of a zone with low V_s and high V_p/V_s (Fig. 6d and e) in the upper crust above the SW-dipping underthrust interface (Fig. 6a, black

dashed line). The low-velocity anomaly can be explained by thermal and/or compositional variation (due to magmatism) and deformational fabric (Zhang et al., 2009). Based on the tectonic history of the Tibetan Plateau, the imaged low-velocity zone can be indicative of a weak zone formed from the acceleration and reorientation of deformation with dominant crust shortening in the northeastern Tibetan Plateau since ~15 Myr (Lease et al., 2012; Meyer et al., 1998; Yuan et al., 2013). The magnetotelluric (MT) survey and other seismological studies reported the presence of fluid and/or partial melt at mid-crustal depth in the India-Asia collision zone (e.g., Caldwell et al., 2013; Wei et al., 2014).

The negative-amplitude signals between depths of 70–170 km in the migration image of the S receiver functions (Fig. 5b) were interpreted as the lithospheric discontinuities based on a previous observation reported in the northeastern Tibetan Plateau (Shen et al., 2015) and other continental lithosphere (e.g., Eaton et al., 2009; Abt et al., 2010; Kumar et al., 2012). The negative-amplitude signal is observed particularly strong with large depth variation across Lenglong Ling to the NE, but weak beneath the Tibetan Plateau (Fig. 5b). In particular, the strong-amplitude signal at ~170 km depth beneath the NE of Lenglong Ling coincides with the depth for LAB constrained from the regional V_s model (An and Shi, 2006). The contrasting amplitude of the lithospheric discontinuities across Lenglong Ling can be attributed to large velocity variation within the mantle lithosphere primarily due to different temperature

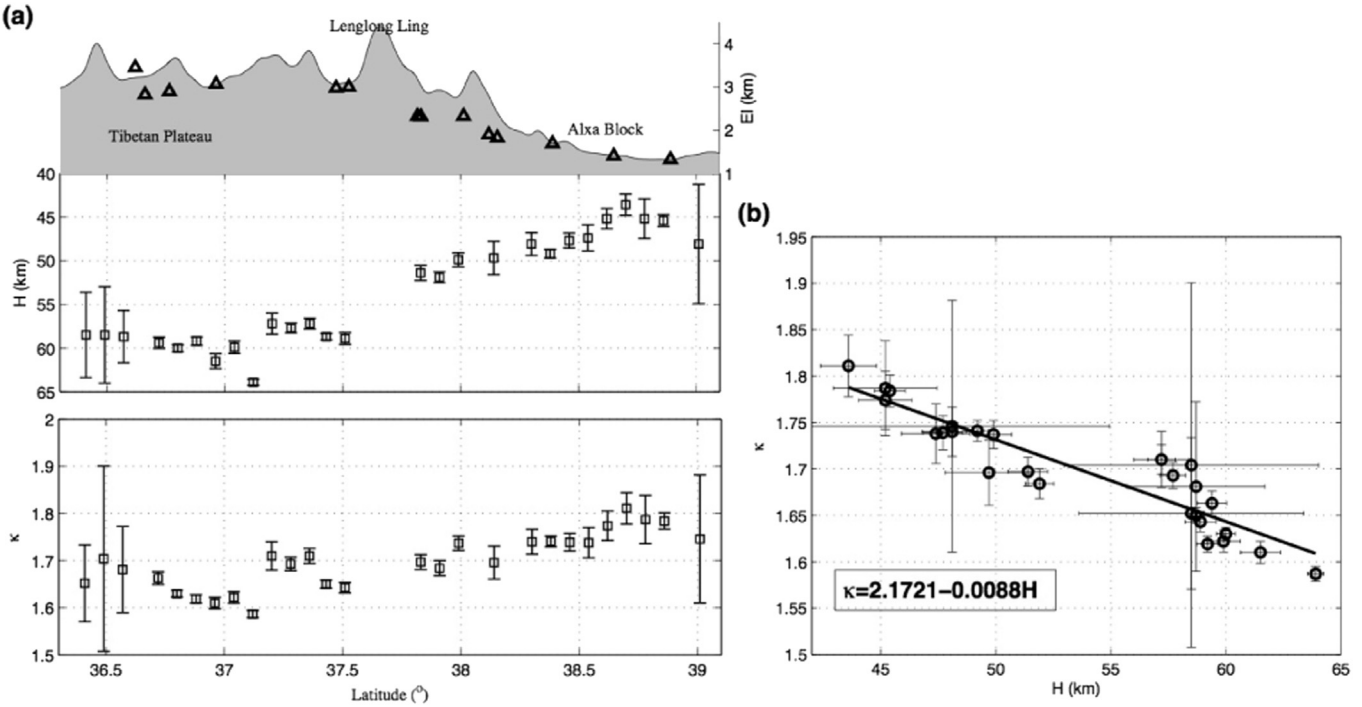


Fig. 8. Crustal thickness (H) and velocity ratio (κ , V_p/V_s) along the seismic profile. (a) H and κ , calculated from the arrival times of Pms and $PpPms$ phases shown in Fig. 7. (b) Relationship between crustal thickness (H) and velocity ratio (κ , V_p/V_s). Plotted data are described by a linear equation shown in the graph.

conditions (Karato, 2012). This inference is supported by previous tomography results (Liang and Song, 2006; Fu et al., 2010; Liang et al., 2012), which suggest that the mantle lithosphere and asthenosphere beneath eastern Tibet is hotter than that of the Asian continent. In addition to temperature, water content (e.g., Karato, 1986) and/or partial melting (e.g., Kawakatsu et al., 2009) may also affect the seismic properties of the lithospheric discontinuities.

6.2. V_p/V_s variation in the northeastern Tibetan Plateau

The V_p/V_s (or Poisson's ratio) can constrain important bounds on the composition of the crust because it is less sensitive to the variations of pressure and temperature than individual V_p or V_s (Christensen, 1996). The contrasting crustal thickness and V_p/V_s across Lenglong Ling (at the latitude of 37.7°) along the A-A' profile (Fig. 3a) imply considerable differences in crustal composition. The bulk crustal composition of the Alxa block in the northeast Lenglong Ling is constrained by the average velocity ratio of 1.744 ± 0.038 , which is close to the average value of the typical stable continental crust (1.768 ; Christensen and Mooney, 1995). On the other hand, the velocity ratio of the region SW of Lenglong Ling (the average value of 1.655 ± 0.040) is significantly smaller than the average value of the continental crust (Christensen and Mooney, 1995). In general, the V_p/V_s is larger than 1.70 for most minerals except Quartzite, which has the velocity ratio of ~ 1.48 (Christensen, 1996). Thus, the lower velocity ratio in the region SW of Lenglong Ling can be explained by the presence of quartz-rich, felsic composition crust. Similar interpretation has been suggested to explain seismic crustal properties (low mean V_p and low Poisson's ratio) beneath the Altiplano of South America, where the crustal thickness ranges from 75 to 80 km and the average velocity ratio is 1.6 (Zandt et al., 1994).

The presence of the quartz-rich component within the crust in the region SW of Lenglong Ling can be also supported by the inverse relationship between the crustal thickness and the velocity ratio (Fig. 8b). This suggests rich felsic-component crust with increasing crustal thickness (Christensen, 1996; Tian and Zhang, 2013).

Although still controversial, crustal shortening and thickening are known as one predominant mechanism (Clark, 2012; Lease et al., 2012) that explain the uplift of the Tibetan Plateau as evidenced by GPS measurements over ten years (Liang et al., 2013). The core problem of the model for crustal shortening and thickening has some ambiguity where the dominant deformation occurred (i.e., upper or lower crust), and how the deformation occurred (Zhao and Morgan, 1987; Clark and Royden, 2000; Tian and Zhang, 2013). The GPS-derived horizontal velocity field relative to the Eurasia-fixed reference frame shows that the velocity of Tibetan crust slows down sharply from south to north, causing strong shortening between India and Eurasia as well as an apparent lateral extrusion (Liang et al., 2013). In particular, the velocity pattern in the southeastern plateau reflects strong lateral extrusion and continuous deformation of the upper crust of the Tibetan Plateau (Liang et al., 2013). Based on this geodetic evidence and the presence of the dipping low-velocity zone above the intracrustal underthrust (Fig. 6), we suspect that more predominant presence of quartz might be present in the upper crust, and we argue that significant deformation is only limited in the upper crust in the northeastern Tibetan Plateau.

6.3. Preferred model for the northeastern Tibetan Plateau

The northeastward lateral growth of the Tibetan Plateau has been resisted by the Asian blocks (e.g., Alxa and Ordos), and has produced prominent left-lateral strike-slip faults, including the Haiyuan fault, Altyn fault, and other thrust faults developed in Qilian Shan (Fig. 1a; Yuan et al., 2013). Such active major faults have produced large earthquakes including the 1920 M 8.7 Haiyuan earthquake in the region. Many sporadic thrust faults have also developed parallel to the Qilian Shan mountain range, and caused numerous moderate-size thrust earthquakes (Yuan et al., 2013). The thrust faulting earthquakes are suggested to be controlled mainly by local stress accumulation associated with upper crustal deformation (Chen et al., 2016). The occurrence of the repeating earthquakes at Lenglong Ling might be related with the latest deformation within the upper crust. The process of crustal thickening here is complex (i.e., Yuan et al., 2013), and can be interrupted by frictional and stress heterogeneity with variable depth (as evidenced

in the subduction zone megathrust fault; e.g., Huang et al., 2012; Lay et al., 2012), which resulted in the complicated crustal structures imaged with receiver functions (Figs. 5a and 6a). Low seismic velocities in our images (Figs. 5a and 6a) are indicative of the presence of fluids and fluid migration within the crust, which can contribute to the variations in frictions and stress heterogeneity (Huang et al., 2012; Lay et al., 2012; Duputel et al., 2016).

Based on our seismic and previous geodetic observation (Chen et al., 2016), we present our preferred model that shows the localized upper crustal deformation in the northeastern Tibetan Plateau (Fig. 9). Our results indicate that the foreland of the Qilian Shan is the onset of the underthrusting upper crust of the Asian blocks. Dominant compressive tectonic stress within the underthrusting upper crust results in dominant thrust-faulting earthquakes (e.g., repeating Menyuan earthquakes). Based on the six years of GPS data, the earthquake source region has experienced substantial changes in stress state from compression to dilatation prior to the earthquake occurrence, reflecting nonlinear adjustment of stress-strain accumulation (Chen et al., 2016). In addition, the GPS crustal strain rate around Lenglong Ling is considerably larger than other regions of the Qilian-Haiyuan fault system (Chen et al., 2016), which might be in part related to the contrasting crustal structures and properties (Figs. 5a, 6, and 8). The shortening rate across Lenglong Ling is up to ~4 mm/yr in the NE-SW direction, indicating the tendency to accumulate stress and the cause of earthquakes. In a 25 km × 25 km area around the epicenter region, the seismic moment accumulation rate derived from GPS crustal strain rates (Savage and Svart, 1997) is about 2.72×10^{16} Nm/yr, which means the strain energy of an event with moment magnitude of about 5.9 could be accumulated in the upper crust in about 33 yr.

Previous models for the formation of the plateau, mostly based on geological investigations, predict major deformation in a crustal and/or lithospheric scale occurring in the northern boundary of the Tibetan Plateau due to the mechanisms of subduction (underthrusting) of the Asian lithosphere under the Tibetan Plateau (Tapponnier et al., 2001; Yin et al., 2008a, 2008b), lower-crustal flow (Royden et al., 1997; Clark and Royden, 2000), or crustal shortening (Dewey et al., 1988; Meyer et al., 1998). Based on our imaged structures from the teleseismic phases and geodetic observation (Chen et al., 2016), we suggest that the crustal shortening model may better represent complicated tectonic and fault structures, and seismicity in the northeastern Tibetan Plateau. The localized deformation in the upper crust is manifested in the repeating earthquakes in Menyuan, the observed dipping structures within

the crust with opposite directions across Lenglong Ling (e.g., the SW-dipping structure in the NE of Lenglong Ling, and the NE-dipping low-velocity layer in the SE of Leonglong Ling; Fig. 6a) and the higher crustal strain rate (Chen et al., 2016). The observed SW-dipping feature indicates that the upper crust of the Alxa block underthrust towards the Tibetan Plateau beneath the foreland of the Qilian Shan mountain range. The similar underthrusting feature is observed in the west Qilian Shan along the profile of wide-angle reflection and refraction studies (Zeng et al., 1998; Gao et al., 1999). Also in the west of our study region, Zheng et al. (2013) report a presence of NE-dipping faults based on field investigations and suggest that those fault systems were developed in conjunction with the northeastward growth of the Tibetan Plateau. Our imaged NE-dipping structure can be thus an indicator of the tectonic response adjacent to neighboring continental blocks in response to the lateral growth of the northeastern Tibetan Plateau, and also control the seismicity of the Qilian Shan thrust belt.

7. Conclusions

We provide teleseismic constraints on the continental collision zone along the SW-NE profile in the northeastern margin of the Tibetan Plateau. The profile crosses the Qilian Shan thrust belt, which is a zone of intense earthquake activity, including a pair of M_w 5.9 earthquakes with a 30-year time interval that occurred in the city of Menyuan near Lenglong Ling. Nearly perfect consistency between the two earthquake waveforms and their similar focal locations demonstrate that the two events are repeating earthquakes. Both P- and S-wave receiver-function images show the contrasting crustal structure and seismic properties across the earthquake source region in Lenglong Ling. High-frequency P receiver functions clearly show a SW-dipping underthrusted upper crust beneath the foreland of the Qilian Shan thrust belt. Also, an imaged strong, NE-dipping, low-velocity layer beneath southwest Lenglong Ling may represent a mechanically weak zone developed by dominant crust shortening in the northeastern Tibetan Plateau since ~15 Myr. Our analysis results argue for localized upper-crustal deformation beneath southwest Lenglong Ling, which is also supported by the shortening rate from GPS. Furthermore, GPS data suggest that the occurrence of the M_w 5.9 earthquake requires the strain energy accumulated in the upper crust for about 33 yr in Lenglong Ling. The upper-crustal deformation in Lenglong Ling can be direct evidence of the lateral growth of the northeastern Tibetan Plateau, and control the seismicity of the Qilian Shan thrust belt.

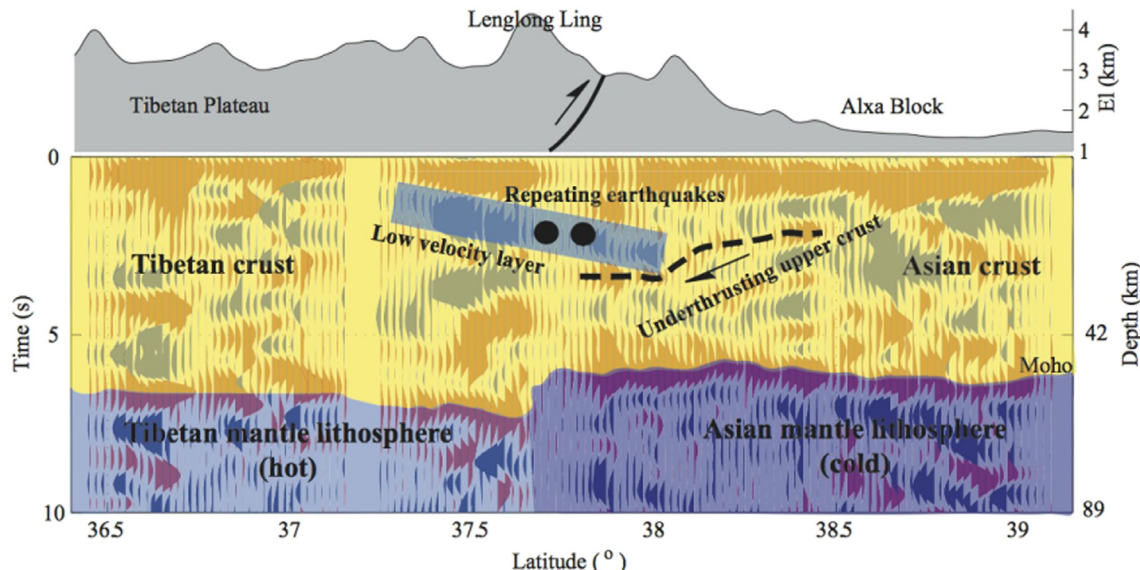


Fig. 9. Our preferred tectonic model showing localized upper-crustal deformation around the repeating source region based on the teleseismic constraints. Arrows indicate the motion of thrust fault system (in the foreland of Qilian Shan) and the motion of underthrusted upper crust. The physical state of the lithosphere is inferred from the work by Shen et al. (2015).

Acknowledgements

X. Shen acknowledges Creative-Pioneering Researchers Program through Seoul National University (SNU SRnD 3345-20160014) National Natural Science Foundation of China (Grants 41574077 and 41274093) and the Basic Research Project of Institute of Earthquake Science of CEA (Grant 2014IESLZ03). Y. Kim acknowledges the National Research Foundation of Korea Grant funded by the Korean Government (NRF-2014S1A2A2027609), and by Creative-Pioneering Researchers Program through Seoul National University (SNU). Waveform data of permanent seismic stations for this study were provided by Data Management Centre of China National Seismic Network at Institute of Geophysics, China Earthquake Administration (SEISDMC, doi:[10.11998/SeisDmc/SN](https://doi.org/10.11998/SeisDmc/SN)). Some figures were plotted with Generic Mapping Tools (Wessel and Smith, 1995), and computations were done in Seismic Handler (K. Stammmer). Dr. Weipeng Ge in Lanzhou Institute Seismology helped to improve the quality of the figures. Finally, authors thank the editor Dr. Kelin Wang and two reviewers for comments that greatly improved this paper.

References

- Abt, D.L., Fischer, K.M., French, S.W., Ford, H.A., Yuan, H., Romanowicz, B., 2010. North American lithosphere discontinuity structure imaged by Ps and Sp receiver functions. *J. Geophys. Res.* 115. <http://dx.doi.org/10.1029/2009JB00691>.
- An, M., Shi, Y., 2006. Lithospheric thickness of the Chinese continent. *Phys. Earth Planet. Inter.* 159 (3–4):257–266. <http://dx.doi.org/10.1016/j.pepi.2006.08.002>.
- Caldwell, W.B., Klempner, S.L., Lawrence, J.F., Rai, S.S., Ashish, 2013. Characterizing the Main Himalayan Thrust in the Garhwal Himalaya, India with receiver function CCP stacking. *Earth Planet. Sci. Lett.* 367, 15–27.
- Chen, W., Gan, W., Xiao, G., Wang, Y., Lian, W., Liang, S., Zhang, K., 2016. Characteristics of regional crustal deformation before 2016 Menyuan Ms 6.4 earthquake. *Geodesy Geodyn.* 7 (4), 275–283.
- Christensen, N.I., 1996. Poisson's ratio and crustal seismology. *J. Geophys. Res.* 101: 3139–3156. <http://dx.doi.org/10.1029/95JB03446>.
- Christensen, N.I., Mooney, W.D., 1995. Seismic velocity structure and composition of the continental crust: a global view. *J. Geophys. Res.* 100 (B6), 9761–9788.
- Clark, M.K., 2012. Continental collision slowing due to viscous mantle lithosphere rather than topography. *Nature* 483, 74–77.
- Clark, M.K., Royden, L.H., 2000. Topographic ooze: building the eastern margin of Tibet by lower crustal flow. *Geology* 28, 703–706.
- Deng, Q., Zhang, P., Ran, Y., Yang, X., Min, W., Chu, Q., 2003. Basic characteristics of active tectonics of China. *Sci. China. Ser. D Earth Sci.* 46 (4), 356–372.
- Dewey, J.F., Shackleton, R.M., Chang, C., Sun, Y., 1988. The tectonic evolution of the Tibetan Plateau. *Philos. Trans. R. Soc. Lond. A* 327, 379–413.
- Duputzel, Z., Vergne, J., Rivera, L., Wittlinger, G., Farra, V., Hetényi, G., 2016. The 2015 Gorkha earthquake: a large event illuminating the Main Himalayan Thrust fault. *Geophys. Res. Lett.* 43:2517–2525. <http://dx.doi.org/10.1002/2016GL068083>.
- Eaton, D., Darbyshire, F., Evans, R., Grüter, H., Jones, A., Yuan, X., 2009. The elusive lithosphere–asthenosphere boundary (LAB) beneath cratons. *Lithos* 109 (1), 1–22.
- Efron, B., Tibshirani, R.J., 1998. *An Introduction to the Bootstrap*. 1998. Chapman & Hall (436 pp.).
- Fu, Y., Li, A., Chen, Y., 2010. Crustal and upper mantle structure of southeast Tibet from Rayleigh wave tomography. *J. Geophys. Res.* 115 (B12323). <http://dx.doi.org/10.1029/2009JB007160>.
- Gan, W., Zhang, P., Shen, Z., Niu, Z., Wang, M., Wan, Y., Zhou, D., Cheng, J., 2007. Present-day crustal motion within the Tibetan Plateau inferred from GPS measurements. *J. Geophys. Res.* 112 (B8).
- Gao, R., Cheng, X., Wu, G., 1999. Lithospheric structure and geodynamic model of the Golmud–Ejin transect in northern Tibet. *Geol. Soc. Am. Spec. Pap.* 328, 9–17.
- Gaudemer, Y., Tapponnier, P., Meyer, B., Peltzer, G., Shunmin, G., Zhitai, C., Cifuentes, I., 1995. Partitioning of crustal slip between linked, active faults in the eastern Qilian Shan, and evidence for a major seismic gap, the 'Tianzhu gap', on the western Haiyuan Fault, Gansu (China). *Geophys. J. Int.* 120, 599–645.
- Hao, M., Qin, S., Li, Y., Wang, Q., Zhou, L., 2014. Recent horizontal velocity field of northeastern Tibetan Plateau. *J. Geodesy Geodyn.* 34 (3), 99–103.
- Hensch, M., Lund, B., Árnadóttir, T., Brändádóttir, B., 2016. Temporal stress changes associated with the 2008 May 29 MW 6 earthquake doublet in the western South Iceland Seismic Zone. *Geophys. J. Int.* 204 (1), 544–554.
- Huang, Y., Meng, L., Ampuero, J., 2012. A dynamic model of the frequency-dependent rupture process of the 2011 Tohoku-Oki earthquake. *Earth Planets Space* 64 (12), 1061–1066.
- Karato, S., 1986. Does partial melting reduce the creep strength of the upper mantle? *Nature* 319, 309–310.
- Karato, S.-I., 2012. On the origin of the asthenosphere. *Earth Planet. Sci. Lett.* 321–322, 95–103.
- Kawakatsu, H., Kumar, P., Takei, Y., Shinohara, M., Kanazawa, T., Araki, E., Suyehiro, K., 2009. Seismic evidence for sharp lithosphere–asthenosphere boundaries of oceanic plates. *Science* 324, 499–502.
- Kennett, B., Engdahl, R., 1991. Travel times for global earthquake location and phase identification. *Geophys. J. Int.* 105, 429–465.
- Kumar, P., Yuan, X., Kind, R., Ni, J., 2006. Imaging the colliding Indian and Asian lithospheric plates beneath Tibet. *J. Geophys. Res.* 111 (B06308). <http://dx.doi.org/10.1029/2005JB003930>.
- Kumar, P., Kind, R., Yuan, X., Mechie, J., 2012. USArray receiver function images of the lithosphere–asthenosphere boundary. *Seismol. Res. Lett.* 83 (3), 486–491.
- Langston, C.A., 1979. Structure under Mount Rainier, Washington, inferred from teleseismic body waves. *J. Geophys. Res.* 84, 4749–4762.
- Lay, T., Kanamori, H., Ammon, C., Koper, K., Hutko, A., Ye, L., Yue, H., Rushing, T., 2012. Depth-varying rupture properties of subduction zone megathrust faults. *J. Geophys. Res.* 117 (B04311). <http://dx.doi.org/10.1029/2011JB009133>.
- Lease, R., Burbank, D., Zhang, H., Liu, J., Yuan, D., 2012. Cenozoic shortening budget for the northeastern edge of the Tibetan Plateau: is lower crustal flow necessary? *Tectonics* 31 (3). <http://dx.doi.org/10.1029/2011TC003066>.
- Li, Y., Gan, W., Wang, Y., Chen, W., Liang, S., Zhang, K., Zhang, Y., 2016. Seismogenic structure of the 2016 Ms 6.4 Menyuan earthquake and its effect on the Tianzhu seismic gap. *Geodesy Geodyn.* 7 (4), 230–236.
- Liang, C., Song, X., 2006. A low velocity belt beneath northern and eastern Tibetan Plateau from Pn tomography. *Geophys. Res. Lett.* 33 (L22306). <http://dx.doi.org/10.1029/2006GL027926>.
- Liang, X., Sandvol, E., Chen, J., Hearn, T., Ni, J., Klempner, S., Shen, Y., Tilman, F., 2012. A complex Tibetan upper mantle: a fragmented Indian slab and no south-verging subduction of Eurasian lithosphere. *Earth Planet. Sci. Lett.* 333–334:101–111. <http://dx.doi.org/10.1016/j.epsl.2012.03.036>.
- Liang, S., Gan, W., Shen, C., Xiao, G., Liu, J., Chen, W., Ding, X., Zhou, D., 2013. Three-dimensional velocity field of present-day crustal motion of the Tibetan Plateau derived from GPS measurements. *J. Geophys. Res.* 118:5722–5732. <http://dx.doi.org/10.1029/2013JB010503>.
- Meyer, B., Tapponnier, P., Bourjot, L., Métivier, F., Gaudemer, Y., Peltzer, G., Shunmin, G., Chen, Z., 1998. Crustal thickening in Gansu–Qinghai, lithospheric mantle subduction, and oblique strike-slip controlled growth of the Tibet plateau. *Geophys. J. Int.* 135, 1–47.
- Nabelek, J., Hetényi, G., Vergne, J., Sapkota, S., Kafle, B., Jiang, M., Su, H., Chen, J., Huang, B., Team, T., 2009. Underplating in the Himalaya–Tibet collision zone revealed by the HiCLIMB experiment. *Science* 325 (5946), 1371–1374.
- Pan, S., Niu, F., 2011. Large contrasts in crustal structure and composition between the Ordos plateau and the NE Tibetan plateau from receiver function analysis. *Earth Planet. Sci. Lett.* 303 (3), 291–298.
- Royden, L., Burchfiel, B., King, R., Wang, E., Chen, Z., Shen, F., Liu, Y., 1997. Surface deformation and lower crustal flow in eastern Tibet. *Science* 276:788–790. <http://dx.doi.org/10.1126/science.276.5313.788>.
- Savage, J., Svart, J., 1997. Postseismic deformation associated with the 1992 Mw = 7.3 Landers earthquake, southern California. *J. Geophys. Res.* 102 (B4). <http://dx.doi.org/10.1029/97JB00210>.
- Shen, X., Zhou, H., 2009. The low-velocity layer at the depth of 620 km beneath Northeast China. *Chin. Sci. Bull.* 54 (17), 3067–3075.
- Shen, X., Mei, X., Zhang, Y., 2011. The crustal and upper-mantle structures beneath the northeastern margin of Tibet. *Bull. Seismol. Soc. Am.* 101 (6), 2782–2795.
- Shen, X., Yuan, X., Liu, M., 2015. Is the Asian lithosphere underthrusting beneath north-eastern Tibetan Plateau? Insights from seismic receiver functions. *Earth Planet. Sci. Lett.* 428, 172–180.
- Shen, X., Liu, M., Gao, Y., Wang, W., Shi, Y., An, M., Zhang, Y., Liu, X., 2017. Lithosphere structure across the northeastern margin of the Tibetan Plateau: implications for the plateau's lateral growth. *Earth Planet. Sci. Lett.* 459, 80–92.
- Sieh, K., 1996. The repetition of large-earthquake ruptures. *Proc. Natl. Acad. Sci. U. S. A.* 93, 3764–3771.
- Stein, R., King, G., Rundle, J., 1988. The growth of geological structures by repeated earthquakes 2. Field examples of continental dip-slip faults. *J. Geophys. Res.* 93 (B11), 13319–13331.
- Tapponnier, P., Peltzer, G., LeDain, A.Y., Armijo, R., Cobbold, P., 1982. Propagating extrusion tectonics in Asia: new insights from simple experiments with plasticine. *Geology* 10, 611–616.
- Tapponnier, P., Xu, Z., Roger, F., Meyer, B., Amaud, N., Wittlinger, G., Yang, J., 2001. Oblique stepwise rise and growth of the Tibet plateau. *Science* 294, 1671–1677.
- Tian, X., Zhang, Z., 2013. Bulk crustal properties in NE Tibet and their implications for deformation model. *Gondwana Res.* 24 (2), 548–559.
- Tian, X., Liu, Z., Si, S., Zhang, Z., 2014. The crustal thickness of NE Tibet and its implication for crustal shortening. *Tectonophysics* 634, 198–207.
- Vidale, J., Ellsworth, W.L., Cole, A., Marone, C., 1994. Variations in rupture process with recurrence interval in a repeated small earthquake. *Nature* 368, 624–626.
- Wang, C., Zhu, L., Lou, H., Huang, B., Yao, Z., Luo, X., 2010. Crustal thicknesses and Poisson's ratios in the eastern Tibetan Plateau and their tectonic implications. *J. Geophys. Res.* 115 (B11).
- Wei, W., Le Page, F., Jones, A., Vozar, J., Dong, H., Unsworth, M., Jin, S., Ye, G., Jing, J., Zhang, L., Xie, C., 2014. Northward channel flow in northern Tibet revealed from 3D magnetotelluric modeling. *Phys. Earth Planet. Inter.* 235, 13–24.
- Wessel, P., Smith, W., 1995. New version of the generic mapping tools released. *EOS Trans. Am. Geophys. Union* 76, 329.
- Yin, A., Harrison, T.M., 2000. Geologic evolution of the Himalayan–Tibetan orogeny. *Annu. Rev. Earth Planet. Sci.* 28, 211–280.
- Yin, A., Dang, Y., Wang, L., Jiang, W., Zhou, S., Chen, X., Gehrels, G., McRivette, M., 2008a. Cenozoic tectonic evolution of Qaidam basin and its surrounding regions (part 1): the southern Qilian Shan–Nan Shan thrust belt and northern Qaidam basin. *Bull. Seismol. Soc. Am.* 120 (7–8), 813–846.
- Yin, A., Dang, Y., Zhang, M., Chen, X., McRivette, M., 2008b. Cenozoic tectonic evolution of the Qaidam basin and its surrounding regions (part 3): structural geology, sedimentation, and regional tectonic reconstruction. *Geol. Soc. Am. Bull.* 120 (7–8), 847–876.

- Yuan, X., Kind, R., Li, X., Wang, R., 2006. The S receiver functions: synthetics and data example. *Geophys. J. Int.* 165, 555–564.
- Yuan, D., Ge, W., Chen, Z., Li, C., Wang, Z., Zhang, H., Zhang, P., Zheng, D., Zheng, W., Craddock, W., Dayem, K., Duvall, A., Hough, B., Lease, R., Champagnac, J., Burbank, D., Clark, M., Farley, K., Garzione, C., Kirby, E., Molnar, P., Roe, G., 2013. The growth of northeastern Tibet and its relevance to large-scale continental geodynamics: a review of recent studies. *Tectonics* 32:1358–1370. <http://dx.doi.org/10.1002/tect.20081>.
- Zandt, G., Velasco, A., Beck, S., 1994. Composition and thickness of the southern Altiplano crust, Bolivia. *Geology* 22 (11), 1003–1006.
- Zeng, R., Ding, Z., Wu, Q., 1998. The crustal structures from Himalaya to Qilian and its implications for continent-continent collision process. *Acta Geophys. Sin.* 41, 48–60.
- Zhang, Q., Sandvol, E., Liu, M., 2009. Lithospheric velocity structure of the New Madrid seismic zone: a joint teleseismic and local P tomographic study. *Geophys. Res. Lett.* 36 (L11305). <http://dx.doi.org/10.1029/2009GL037687>.
- Zhao, W., Morgan, W., 1987. Injection of Indian crust into Tibetan lower crust—a two-dimensional finite-element model study. *Tectonics* 6, 489–504.
- Zhao, J., Yuan, X., Liu, H., Kumar, P., Pei, S., Kind, R., Zhang, Z., Teng, J., Ding, L., Gao, X., Xu, Q., Wang, W., 2010. The boundary between the Indian and Asian tectonic plates below Tibet. *Proc. Natl. Acad. Sci.* 107:11229–11233. <http://dx.doi.org/10.1073/pnas.1001921107>.
- Zheng, W., Zhang, P., Ge, W., Molnar, P., Zhang, H., Yuan, D., Liu, J., 2013. Late Quaternary slip rate of the South Heli Shan Fault (northern Hexi Corridor, NW China) and its implications for northeastward growth of the Tibetan Plateau. *Tectonics* 32, 271–293.
- Zheng, D., Li, H., Shen, Y., Tan, J., Ouyang, L., Li, X., 2016. Crustal and upper mantle structure beneath the northeastern Tibetan Plateau from joint analysis of receiver functions and Rayleigh wave dispersions. *Geophys. J. Int.* 204, 583–590.